11-2023

Multicolor Dye-based Flow Structure Visualization for seal-whisker geometry characterized by computer vision

Ondřej Ferčák
Portland State University

Kathleen Lyons
University of Wisconsin

Christin T. Murphy
Naval Undersea Warfare Center Division Newport

Kristina M. Kamensky
Naval Undersea Warfare Center Division Newport

Raul Bayoan Cal
Portland State University, rcal@pdx.edu

Citation Details

Multicolor dye-based flow structure visualization for seal-whisker geometry characterized by computer vision

1
2
3
4
5
6
7
8
9
10
11
12
13
14
15
16
17
18
19
20
21
22
23
24
25
26
27
28
29
30
31
32
33
34
35
36
37
38
39
40
41
42
43
44
45
46
47
48
49
50
51
52
53
54
55
56
57
58
59
60

Multicolor dye-based flow structure visualization for seal-whisker geometry characterized by computer vision

Ondřej Ferčák[†]**, Kathleen M. Lyons**[‡]**, Christin T. Murphy**[§]**, Kristina M. Kamensky**[§]**, Raúl Bayoán Cal**[†]**, and Jennifer A. Franck**[‡]

†Department of Mechanical & Materials Engineering,
 Portland State University, Portland OR
‡Department of Engineering Physics,
 University of Wisconsin–Madison, Madison WI
§Naval Undersea Warfare Center Division Newport,
 Newport RI

E-mail: `ofercak@pdx.edu`[†]

Abstract.

Pinniped vibrissae possess a unique and complex three-dimensional topography, which has beneficial fluid flow characteristics such as substantial reductions in drag, lift, and vortex induced vibration. To understand and leverage these effects, the downstream vortex dynamics must be studied. Dye visualization is a traditional qualitative method of capturing these downstream effects, specifically in comparative biological investigations where complex equipment can be prohibitive. High-fidelity numerical simulations or experimental particle image velocimetry (PIV) are commonplace for quantitative high-resolution flow measurements, but are computationally expensive, require costly equipment, and can have limited measurement windows. This study establishes a method for extracting quantitative data from standard dye visualization experiments on seal whisker geometries by leveraging novel but intuitive computer vision techniques, which maintain simplicity and an advantageous large experimental viewing window while automating the extraction of vortex frequency, position, and advection. Results are compared to direct numerical simulation (DNS) data for comparable geometries. Power spectra and Strouhal numbers show consistent behavior between methods for a Reynolds number of 500, with minima at the canonical geometry wavelength of 3.43 and a peak frequency of 0.2 for a Reynolds number of 250. The vortex tracking reveals a clear increase in velocity from roll-up to 3.5 whisker diameters downstream, with a strong overlap with the DNS data but shows steady results beyond the limited DNS window. This investigation provides insight into a valuable bio-inspired engineering model while advancing an analytical methodology that can readily be applied to a broad range of comparative biological studies.

Keywords: Pinniped Vibrissae, Dye-Visualization, Vortex Tracking, Computer Vision

Submitted to: *Bioinspir. Biomim.*

2

1. Introduction

The vibrissae (whiskers) of harbor seals, and most other phocid seal species, are comprised of a pattern of complex three-dimensional undulations which are unique to this group. These undulated contours provide beneficial fluid flow characteristics including substantial drag reduction, oscillating lift force reduction, and shifting vortex-shedding to lower frequencies when compared to smooth profiles [1–4]. The geometric parameters that describe this topography, and the effect they have on flow properties, however, have only recently started to be examined. These studies are mostly comprised of qualitative analog (experimental), or quantitative digital (numerical), methodologies with little to no overlap [3, 5–7]. The present study introduces a hybrid method, which is demonstrated by combining a qualitative dye-visualization experiment with open-source computer vision (CV) techniques, to digitally characterize and quantify flow response over the bio-inspired undulated profiles.

Fluid flow visualizations have relied on human vision for qualitative analysis of water, dye, or smoke flow behavior since the 1400's [8]. This approach has fallen out of favor with the rise of computational power and highly specialized experimental equipment. For example, particle image velocimetry (PIV) and computational fluid dynamics (CFD), can provide extremely detailed quantitative information about the fluid flow far beyond human visual ability. However, PIV requires extensive training, time-consuming setup, and high cost and the increased fidelity of CFD, such as large eddy simulations (LES) and direct numerical simulations (DNS), still have high computational cost and, therefore, require high performance computing systems. On the other hand, dye is still used reliably for fluid visualizations, specifically in comparative biological investigations, like the work of Gilpin et al. [9] who used long exposure dye visualization with a novel open-source software to look at microfluidic structures of starfish larvae [10–14]. Dye has also been used in combination with PIV, simulations, or machine learning such as Raissi et al. [15] who trained a deep-learning framework to recognize velocity and pressure fields from dye and smoke experimental studies [16–18].

The methodology used to characterize the flow response over the pinniped geometry in this study fills a gap between classic dye experimentation and computationally expensive simulations, PIV, or a combination thereof by leveraging readily available, lean, open-source computer vision software. This approach is used in parallel with DNS data for analysis and methodological comparison where applicable.

Research into vibrissae-inspired profiles is relatively new, but investigations into sinusoidal, wavy,

or undulated bluff-bodies utilizing visually inspected photographs, time-exposure photography, and dye visualization have provided insight of potential benefits [19–21]. Some care must be taken when analyzing dye visualized flows since the dye motion can differ from the underlying flow [22, 23]. Nevertheless, dye is invaluable when cost, safety, time, and equipment are prohibitive. Further, the use of multiple dye-colors is a distinct advantage that comparable CFD results have difficulty implementing. The use of multi-color dye has been exploited by researchers to visualize a wide variety of flows [24–27]. Beyond biological studies, aeronautical research often employs the use of multiple dye colors to visualize distinct streak-lines and vortical structures [28–30].

The current work characterizes the effect of seal whisker geometry on coherent vortex structures and proposes several quantitative analysis methods using computer vision (CV) techniques from multi-color dye-based flow videos. First, the whisker-inspired geometries are defined, and details of the computational and experimental setups are presented in the experimental methods section. Then, the quantitative methods are outlined in the data analysis techniques subsections: color segmentation, Lagrangian vortex tracking, and background subtraction. Flow parameters of seal whisker topography and wavelength modifications are investigated in the results section using the dye visualization, computer vision, and CFD methods. The conclusions section includes context and discussion.

2. Experimental Methods

2.1. Model Definition

The baseline undulated elliptical geometry is defined by seven geometric parameter values based on the work of Hanke et al. [1]. The geometric parameters have been redefined and nondimensionalized such that they are independent from one another as detailed in the work by Lyons et al. [5] and are summarized in Figure 1.

Borrowing from aerodynamic terminology, the chord C is the width of the undulated cylinder model in the streamwise direction (x-coordinate) and the thickness T is the width of the model in the transverse direction (y-coordinate) (Figure 1d). The geometry contains two spanwise undulations, one each in chord and thickness, with their own amplitude, A_C and A_T respectively. Both amplitude terms, as well as the periodicity of the geometry, which is governed by the wavelength λ, are normalized by thickness T.

Five whisker geometries are shown in Figure 1; a baseline whisker geometry based on Hanke et al., three additional models with wavelengths varying from the baseline, and an elliptical cylinder with no undulations.

3
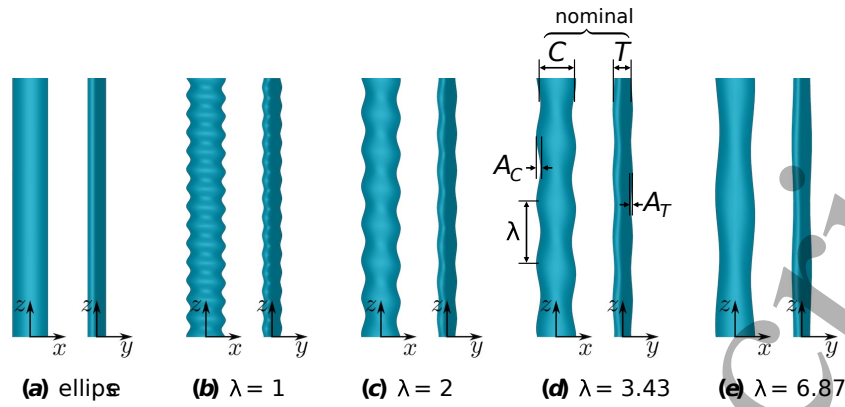
Figure 1. Top and side views of investigated models including smooth ellipse and undulated cylinder geometries with four unique wavelength, λ values, which govern the periodicity. The model corresponding to $\lambda = 3.43$ most closely matches the average measurements obtained from harbor seal whiskers and shows the remaining nondimensionalized parameters that define the seal whisker topography, where C is the average chord length and T is the average thickness. Undulation amplitudes along the chord length and thickness are given by A_C and A_T, respectively.

All other wavelength models share the same normalized values of $AC = 0.23$, $AT = 0.09$, and $T = 1.00$ with only the value of λ changing. The elliptical cylinder has an equivalent aspect ratio of the baseline whisker but no undulation.

To quantify and discuss the results, the response of the flow over the undulated cylinder models is nondimensionalized with respect to the freestream velocity, u_∞, and the mean hydraulic diameter, D_h. The hydraulic diameter for the ellipse is 1.28 and D_h increases (1.27, 1.27, 1.28, and 1.32) along with the respective λ values (1.00, 2.00, 3.43, and 6.87) visualized in Figure 1.

Given the variation in diameter, D_h is calculated using the mean cross-sectional area and perimeter, in the same manner as Witte et al. [2], among others [31,32]. Thus, the Reynolds number is defined as,

$$Re = \frac{U_\infty D_h}{\nu} \tag{1}$$

where ν is the kinematic viscosity of the fluid. The nondimensional time scales of vortex shedding can be characterized by a reduced frequency,

$$f^* = \frac{f D_h}{U_\infty}, \tag{2}$$

where the Strouhal number, St, is defined in this context to be the strongest peak of the force frequency spectra.

2.2. Dye Visualization Setup

The water tunnel in the affiliated lab space is an open channel, 5689 L (1503 gal) recirculating system manufactured by Engineering Laboratory Design. The test section measures 225 cm (L) x 45 cm (W) x 45 cm (H) and is fitted with optical glass. Volumetric

flowrates between 0.6075 - 465.75 L/s and flow velocities between 0.003 - 2.3 m/s are achievable.

Scale models with a mean chord length, C, of 1.32 cm, mean thickness, T, of 0.69 cm, and varying wavelength, λ, are created in clear acrylic resin using a stereolithography 3D printer. Each model is mounted horizontally in the tunnel within the first 50 cm of the test section from struts fixed to the rails at the top of the tunnel. After the model has been installed in the tunnel, coarse and fine adjustment in the vertical and lateral directions can be achieved at several locations in the fixtures for both the model and dye nozzles.
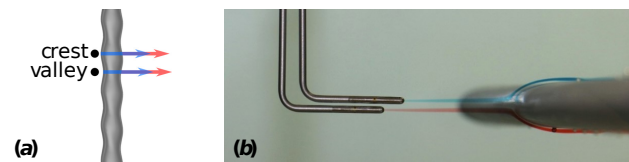
Figure 2. Dye probes release blue and red dye: a) Top view of two spanwise testing locations for each model, leading edge crest and leading edge valley. b) Experimental view of two nozzles releasing blue and red dye.

Red and blue dye are stored in two dye wells above the water tunnel. The dye is gravity fed and continuously released upstream of the model by two nozzles, blue above the center of the cylinder and red below the center of the cylinder, as shown in Figure 2. The composition of the dye is as follows: for every 10 mL of water, one drop each of food coloring and isopropyl alcohol is used. The isopropyl alcohol helps to counteract the increase of density of the added food coloring in order to achieve the same density of water to provide accurate flow visualization. The hydrostatic pressure at the dye outlet is adjusted by modifying the mounting height of the wells above the water

4
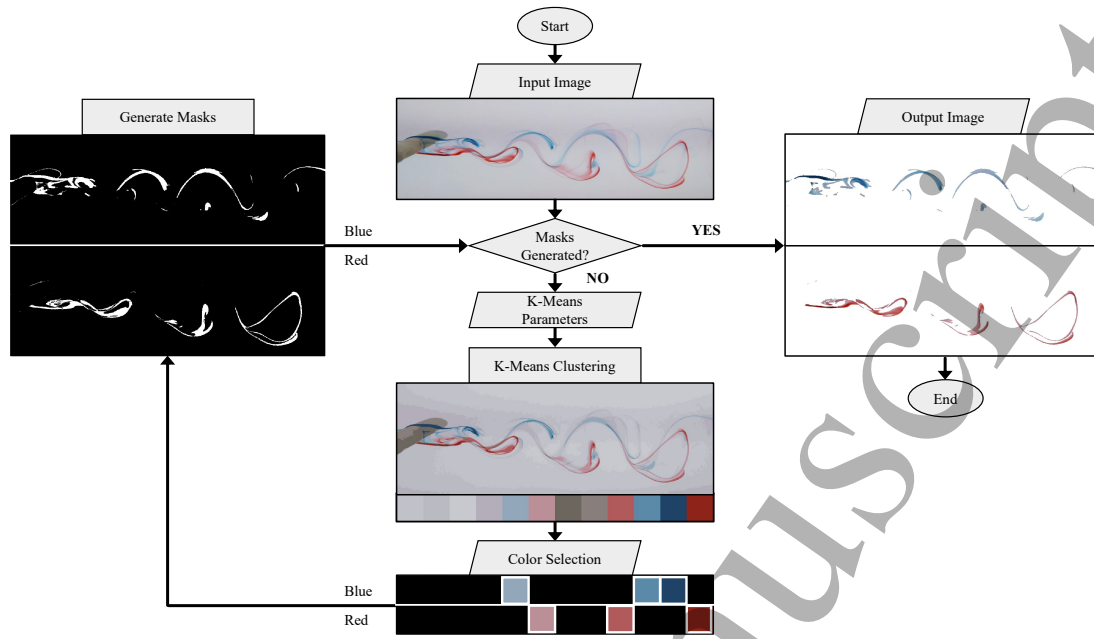
Figure 3. The color segmentation process includes an input image whose color range is binned into a specified number of RGB color ranges using K-means color quantization. The colors are then used to create any number of user defined masks, which are then used on the original image to extract the desired color. Shown here is $\lambda = 6.87$, $Re = 250$, at a peak position.

tunnel. The dye flow is further adjusted by a needle valve attached to each dye well. The location and angle of the dye ports can impact the dye trajectory, thus considerable effort is made to ensure the dye colors advect along the boundary layer. The dye port measures 0.159 cm in diameter and is carefully selected to achieve the necessary dye volumetric flowrate while minimizing flow disturbance.

For each geometry tested, the temperature of the water and the pump speed are measured and recorded. A Canon EOS 80D camera and Photron FASTCAM Mini high-speed camera are used to record video imaging of the dye in the flow over each model and in the near wake region. Each experimental video consists of 5K frames in total, a resolution of 1024 x 512, and a frame rate of 30 frames per second (fps). A typical vortex shedding cycle occurs over 100 frames (e.g. $\lambda = 3.43$, $Re = 500$). While the CV algorithm itself is not affected by the number of frames per cycle, it is preferable to have more than a minimum of 20-30 frames for a typical camera setup. Fewer frames may not be enough to smoothly resolve velocity and acceleration components for vortex advection. A grid poster with known dimensions of 2.5 x 2.5 cm is mounted to the outer backside of the test section to allow for image pixel scaling and help with fixture alignment. Velocity calibration is completed by the manufacturer from the factory using Laser Doppler Velocimetry (LDV). Local velocity is confirmed by highly repeatable timed dye tracking over the test section length of 1.5 m.

Dye visualization data are collected for the baseline model and the three modified configurations, $\lambda = 1.00$, 2.00, 3.43, and 6.87. Each of the models in the current study is observed at two flow speeds. The low speed is equivalent to $Re = 215 - 250$ and are referred to as $Re = 250$ throughout the text as flow variations within this Re range are negligible. Data is also recorded at a second, higher speed flow, approximately equivalent to $Re = 500$. Because the model geometry varies significantly along its span, two spanwise locations are recorded for each configuration. The first recording is taken when the dye is incident on a leading-edge crest and the second is taken when the dye is incident on a leading edge valley. All configurations are tested at zero angle-of-attack with the oncoming flow.

2.3. Data Analysis Techniques: Color Segmentation

The dye visualization videos are analyzed frame-by-frame with standard computer vision methods using an open-source image processing library (OpenCV) in the Python programming language [33]. The methods discussed, however, can easily be implemented via similar libraries in a variety of programming languages.

In order to extract as much relevant data as possible from the images, the primary step in analysis requires either distinguishing the flow in question from the stationary background (background subtraction), or distinguishing the individual dye-colors from each other (color detection), or a combination of both. In

this section, accessible and robust color segmentation methods are discussed, and background subtraction is discussed in the next section.

The concept of isolating red, blue, and green (RGB) pixel intensities (0-255) is relatively simple. However, this task can be fraught with frustration since real world, or experimental, images have a broad range of pixel intensities and overlap, making it difficult to isolate colors in a clean and efficient manner. Human vision is excellent at detecting colors in an image, partly because the distinctions can be compartmentalized, while a computer algorithm treats each pixel as a distinct color. To simulate human interpretation more closely, the colors that are represented in the image are reduced, or clustered, to a chosen total number of colors. This is achieved with a K-means color quantization summarized in Figure 3.

First, the input image, or video frame, is loaded into the software in order to generate a mask for color segmentation. The example used in Figure 3, is that of $\lambda = 6.87$, $Re = 250$, at a peak position. The K-means parameters, including the number of clusters κ, termination criteria ϵ, and optional initialization criteria, are then input to initialize the color quantization. The number of clusters is dependent on the image to be processed and requires some initial testing. Typical values range from $\kappa = 8 - 15$. The K-means algorithm is an iterative algorithm and the termination criteria ϵ may be software dependent but is typically specified as the accuracy of the desired result (i.e. the convergence value of successive iterations). If the change between iterations is less than ϵ, the algorithm will terminate. Other termination parameters can include a maximum iteration (in the case of no convergence) and initialization parameters. This study used $\kappa = 12$ clusters, an accuracy termination criterion ϵ of 0.05, a max iteration criterion of 30, and a center initialization technique based on Arthur et al. [34]. Typical applications can use default termination criteria if included with the respective software library since their changes will be minimal compared to changes in $\kappa = 8 - 15$. Default criteria, for example, can range between ϵ of 0.1-1.0, a maximum iteration criterion of 10-50, and a random center initialization technique.

Once the RGB values are calculated for each of the clusters (e.g. $\kappa = 12$), they can be used for color segmentation as the user chooses. For this study, three separate hues were chosen for both blue and red dye colors as seen in Figure 3. These hue choices are then used to generate masks for the blue and red dyes from the clustered image. The masks are then used on the original image to extract the full range of colors that make up the hues in question. Since the distances

in the image are inherently in pixels, a reference, or calibration, image needs to be taken with an object of known size to establish proper scaling, which is calculated at 0.185 cm/pixel for this study. These extracted colors can now be used for further analysis with respect to shape, size, distance, or motion of the specified dye.

2.4. Data Analysis Techniques: Lagrangian Vortex Tracking

When coherent structures such as vortices are visible in the isolated dye-color images, it is possible to track these structures in a time series of images, making it possible to retrieve a simple Lagrangian tracking algorithm. For this to be effective, it is important to establish a flow that is not overly diffuse and shows structure coherence in the region of interest. In other words, if the dyed vortices are not distinct enough from the background, obscured, or missing such as in Figure 3, they cannot be calculated from flow field vector data such as PIV, even if present. The vortices themselves need to be distinct for computer vision to identify them to obtain the benefits outlined in the methodology of this study. For similar reasons, this study uses the canonical $\lambda = 3.43$ cylinder at Re = 500 for vortex tracking.
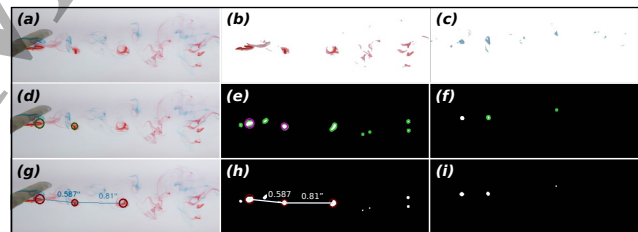
Figure 4. Vortex Identification Process: a) The original image snapshot. b) Red dye segmentation. c) Blue dye segmentation. d) The original image snapshot with vortices highlighted. e) Red segmentation after erosion and dilation. Green highlights the border of remaining structures, and red shows an enclosing circle satisfying the input criteria. f) Blue segmentation showing process described in e. g) The original image snapshot with vortices highlighted and inter-vortex distances displayed. h) Red segmentation showing only the remaining structures and distances. i) Blue segmentation showing process described in h.

For each dye color, the images are first converted to a binary (0 or 255) image for ease of calculations, and a combination of morphological image transformations are used, specifically erosion and dilation, for vortex identification. A 3x3 pixel kernel is used as a structuring element to implement 2D convolution for the following operations. Erosion removes noise in the image and any bordering pixels unbounded by like pixels, effectively shrinking the structures in the image leaving only the dominant ones. Dilation, the inverse to erosion, is then used to make the dominant struc-

tures more robust for further analysis. The surviving structures are fitted with a minimum enclosing circle, which is the smallest circle into which the structure shape can fit and is usually tangent to the structure at several points. This circle can now be used to quantify the roundness, size, and position of each structure as seen in Figure 4.

To minimize outliers during vortex identification, a few reasonable assumptions are used to further filter the structures. These assumptions are parameterized to include each structure's maximum size, minimum size, and roundness. Since there is no machine learning involved in the algorithm, these limits are required in lieu of a more intensive training data set. The maximum and minimum sizes are estimated from initial test images where vortical scales can be visualized, where the minimum size should be large enough as to avoid pixel scale noise (e.g. small dots versus vortices) and the maximum size should be small enough to avoid identification of simultaneous vortices or large-scale dye advection (e.g. large sections of the image). The roundness can easily be estimated by a ratio of areas between the minimum enclosing circle and the structure itself. The closer the ratio is to one, the more round the structure and, therefore, more likely to contain a vortex. These parameters need to be fine-tuned by the user but are intuitive and easy to implement due to the immediate visual feedback. Once the algorithm is established, the minimum enclosing circle centers can be used to quantify vortex position and identification.

2.5. Data Analysis Techniques: Background Subtraction

A complimentary method for extracting dye motion from image frames is background subtraction and is illustrated on a subset of dye data in this study. The input frames (V_{in}) are initially brightened (V_{out}) using inverse gamma correction of the form $V_{out} = V_{in}^{1/2}$ seen in Figure 5a. To differentiate the dye from the background, each frame is compared with previous frames to establish changing and stationary portions of the image.

The algorithm implemented in this study utilizes an improved adaptive mixture of Gaussians (MOG) based model as described by Zivkovic et al. [35, 36]. The resulting frames show only the dye motion and are converted, where the resulting mask pixel values are black (0) for stationary pixels and white (255) for pixel motion similar to the previous masks (Figure 5). The mask pixels known to be outside of the dye wake are forced to black to avoid outlier noise. Any singular pixel outliers are removed through a median blur, which is a 2D convolution with a 7x7 kernel used to replace a pixel value with a median value.
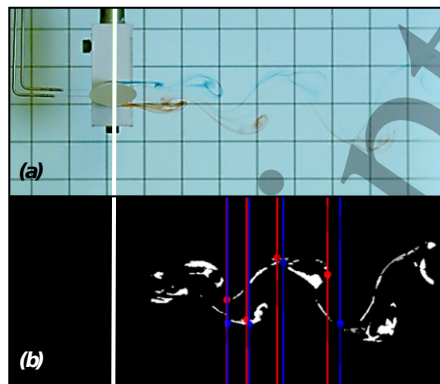
Figure 5. Frequency analysis process: a) Image initialization with brightness optimization, assignment of a streamwise cylinder-centered datum (white line), and mask creation. b) Mask with red and blue line probes to capture upper and lower dye motion.

The masks are then used to calculate frequency spectra by using the vertical motion along the upper and lower edges of the dye. Vertical pixel motion is collected at eight fixed horizontal locations spaced relative to the whisker center, which is indicated by the white line in Figure 5. Four locations are used to capture the upper edge of the wake (red) and four for the lower edge (blue). The eight locations are spaced asymmetrically to prevent wavelength synchronization. The upper probes are placed at x/D_h values of 4.41, 5.20, 6.37, and 8.33 while the lower probes are positioned at 4.45, 5.28, 6.62, and 8.82.

Any outliers or missing positional data are replaced with their preceding values. The power spectral density (PSD) is then calculated using Welch's method using a Hann window size of two-thirds of the data length, a two-thirds overlap, and 10K zero-padding [37]. The eight data sets are then averaged together and peak frequencies above thresholds of 0.1 and 0.35 for $Re = 250$ and $Re = 500$ are documented, respectively.

2.6. Direct Numerical Simulations

The computer vision analysis is compared to the direct numerical simulations (DNS) performed by Lyons et al. [38]. The computations simulate the flow field around the six geometric models investigated, by solving the incompressible Navier-Stokes equations using the open-source software OpenFOAM [39]. Full details on the numerical schemes, mesh resolution, and validation are provided in references Lyons et al. [38] and Yuasa et al. [40] but are summarized here in brevity.

A three-dimensional two-wavelength spanwise periodic computational domain is utilized, simulating an infinite span whisker profile, and neglecting any tip effects. The mesh generation process of Yuasa

et al. [40] maintains a structured body-fitted mesh for the precise undulation geometry. The total mesh size is 4.14M cells for the baseline model, and decreases/increases with respect to wavelength due to the variation in total span across the various models. The results have been previously validated against prior whisker simulation data using the mean drag and RMS lift forces.

3. Results

3.1. Qualitative Observations of Dye Visualization
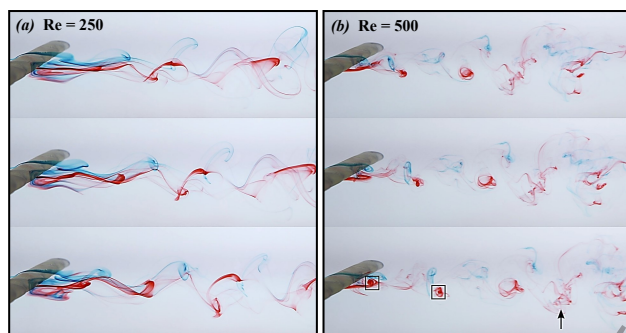
Figure 6. Time progression of flow over the $\lambda = 3.43$ model behind the crest location: a) Dye traces form oscillating shear layers at $Re = 250$. b) At $Re = 500$, dye traces detach and roll up into more coherent vortices before diffusing and dissipating into chaotic structures downstream, marked with boxes and arrow respectively. Frames are chosen to capture a single shedding cycle, therefore time between frames approximately twice as long for $Re = 250$ as for $Re = 500$.

Before discussing computer vision analysis, the flow is qualitatively observed with respect to the two independent variables, Reynolds number Re and wavelength λ, to establish overall trends. Regardless of the geometric whisker model, several differences are apparent when comparing dye traces at different Reynolds numbers. At the lower $Re = 250$, the dye forms shear layers that oscillate in the y-direction as they move downstream. These layers remain largely connected forming wavy filaments in the wake as shown in Figure 6a and Figure 3. These wavy filaments are likely evidence of hairpin vortices, which are more prominently identified from the y-z plane, and are identified in the computational work of Liu et al. among others [1, 38, 41].

At the higher $Re = 500$, the dye traces in the shear layers roll up and detach into more coherent vortices seen boxed in last panel of Figure 6b. A trend of detached structures is consistent across geometric models even though many of the flow patterns diverge from a typical von Kármán vortex street. In the downstream region of the high Re cases, more chaotic structures are visible such

as those near the arrow also shown in Figure 6b), indicating increased turbulent fluctuations. Similar development of turbulent structures has been noted in dye visualization of flow over smooth circular cylinders, which transition to a turbulent wake [19].

3.2. Automated Extraction of Shedding Frequency

Previous dye experiments could only provide a single shedding frequency calculated by manual vortex counting, but with the use of computer vision analysis, a more resolved shedding spectrum is extracted from the unsteady phenomena. Although dye visualization can provide diagnostic cues for assessing the forces on the body, such as formation length and development of turbulent structures, drag and lift force calculations can only be determined through the inclusion of additional experimental sensors or numerical simulation and are thus not included here. A full discussion of lift and drag is detailed in Lyons et al. [38].
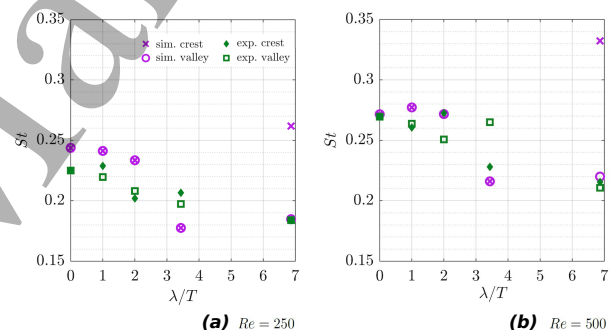
Figure 7. Comparison between calculated shedding frequencies from simulation and those computed from dye visualization video analysis shows a consistent downward trend of St with respect to λ up to $\lambda = 3.43$, the nominal seal whisker wavelength. The spanwise differences for the $\lambda = 6.87$ model are captured within simulation results but are unresolved by the dye visualization analysis.

Using the background subtraction methods described in the data analysis techniques subsection, background subtraction, unsteady flow patterns are quantified through analysis of the dye streaks. Images at both the geometric crest and valley whisker cross-sections are analyzed for all λ profiles at both Reynolds numbers. The PSD is computed for each image sequence, then the dominant, or peak frequency is non-dimensionalized as the Strouhal number (St) number and plotted in Figure 7. Whisker crest and valley data points match well with one another, especially at low Re. At higher Reynolds number, this deviation between crest and valley is larger at the intermediate wavelengths, $\lambda = 2$ and 3.43 but converge again at the highest wavelength.
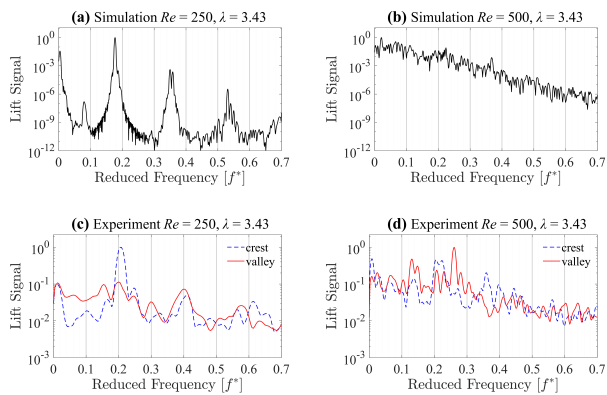
Figure 8. Power spectral density (PSD) for $\lambda = 3.43$ share similar peak shape and location at $Re = 250$ for both simulation (a) and experiment (c). At $Re = 500$, PSD spectra follow a downward slope for both simulation (b) and experiment (d) but lack the distinctive nature of the peaks seen at $Re = 250$, resulting in an imprecise selection of St values for the $\lambda = 3.43$ case at $Re = 500$ and the data spread seen in Figure 7b.
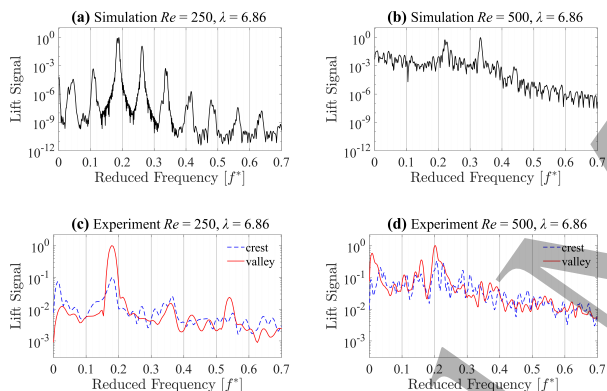
Figure 9. Power spectral density (PSD) for $\lambda = 6.87$ share similar peak shape and location at $Re = 250$ for both simulation (a) and experiment (c), but the simulation reveals additional decreasing peaks on either side at constant frequency intervals. At $Re = 500$, PSD spectra follow a downward slope for both simulation (b) and experiment (d) but while the peaks for the experiment are approximately at the $Re = 250$ range, the magnitudes are small and the simulation is inconsistent.

The global trend for the dye frequencies is a drop in St with respect to λ, consistent across both Reynolds numbers. For comparison the DNS frequency spectra is extracted from a transverse velocity probe directly downstream of the body using the simulation data from Lyons et al. [38], at the same geometric crest and valley locations.

The simulations reveal a similar trend, with the Strouhal number decreasing with respect to wavelength. However, the decrease is more extreme for the DNS data, ranging from $St = 0.242$ to $St = 0.177$, whereas the dye data is $St = 0.228$ to 0.183 for low Re, while at high Re measurements, the dye follows DNS more closely. Furthermore, the

simulations display a rapid decrease between $\lambda = 2$ and 3.43 at both Reynolds numbers, whereas the decrease in experimental measurements is more gradual between $\lambda = 1$ and 3.43.

The simulation data also reveals that the valley and crest locations produce the same dominant frequency for all cases except $\lambda = 6.87$. Both Figure 7a and 7b show the alignment of the purple markers for $\lambda <= 3.43$ and then a sudden diversion at the largest ($\lambda = 6.87$) wavelength. Further inspection of the simulation data at $\lambda = 6.87$ reveals competing frequencies around $f^* = 0.18$ and 0.26 (Figure 9), and both are present at the crest and valley probes, with one slightly stronger than another. The dye visualization calculations are not able to discern the two frequencies along the span, and only pick up the lower of the two frequencies. The simulations are able to maintain perfect symmetry, while the dye data are affected by various real-world factors such as model precision, deviations in angle of attack, intermittent flow instabilities, and background noise in the water tunnel.

The spread between dye calculated frequencies for the $\lambda = 3.43$ at $Re = 500$ and $\lambda = 6.87$ for both Reynolds numbers are larger than observed for the other cases. Therefore, the $\lambda = 3.43$ and $\lambda = 6.87$ case are analyzed in more detail to gain a better understanding of the flow. To fully compare the frequency content contained in collected dye visualization data for $\lambda = 3.43$, a PSD is calculated for the simulated lift signal in the same manner as the dye visualization pixel locations outlined in the background subtraction subsection. The PSD plots for $Re = 250$ in Figures 8a and 8c show distinct peaks near $f^* = 0.2$ for both the simulation and experimental data. A secondary peak in the simulation results near $f^* = 0.35$ also appears in the dye data albeit with a less distinct and broader peak.

For $Re = 500$, the same geometry displays a more complex lift spectra with broad peaks and gentle slopes rather than steep sharp peaks as seen in Figure 8b, and a dominant peak from the simulation data is difficult to discern. The PSD trends for the dye analysis are shown in 8d and follow a similar downward slope at higher frequencies and both plots are noticeably noisier than the $Re = 250$ case.

Similarly, a PSD is calculated for $\lambda = 6.87$ and shown in Figure 9. At $Re = 250$, both the simulation (a) and experimental (c) spectra show large prominent peaks at just under $f^* = 0.2$, including the experimental crest location, albeit with a reduced magnitude. However, the DNS data shows a repeating pattern of large peaks, decreasing in magnitude to either side of the dominant frequency. This behaviour is likely to produce competing frequencies such as the

9
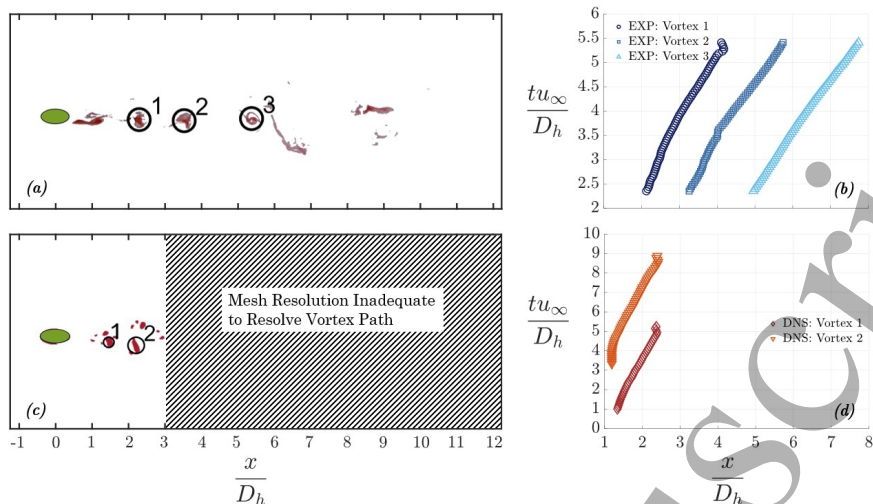
Figure 10. Tracked vortices at position δ_ω/D_h, and convective time, tu_∞/D_h, for $\lambda = 3.43$ and $Re = 500$. (a) Normalized dye position snapshot. (b) Normalized dye position data. (c) Normalized DNS position snapshot (Vertical lines in snapshot indicate region of poor mesh resolution in DNS analysis). (d) Normalized DNS position.

one around $f^* = 0.27$ seen in Figure 9a. The spectra showing $Re = 500$ in Figures 9b and 9d are comparable to the $Re = 500$ data in Figure 8, where a more noisy downward slope is observed. The main distinction between $\lambda = 3.43$ and $\lambda = 6.87$ is that the latter shows more prominent and competing peaks with a higher frequency near $f^* = 0.32$ slightly larger than the other peak near $f^* = 0.22$.

3.3. Lagrangian Vortex Advection

To avoid reliance on user vision and automate vortex identification while limiting computational cost, the Lagrangian vortex identification and tracking algorithm described in the data analysis techniques subsection, Lagrangian vortex tracking is used to track three vortices as they move through time. Figure 10b shows a snapshot of the tracking results and positional data for the red dye. The choice of dye color is arbitrary, and symmetry is assumed for advection of the vortices visualized by the blue dye in the streamwise direction. Vortices show slight displacement in the vertical direction, but this magnitude is negligible compared to the streamwise displacement and will, therefore, be excluded from the following analysis. Vortex 1 (Figure 10) is seen forming behind the whisker and vortices 2 and 3 can be seen advecting at different rates downstream.

The position of each vortex in the streamwise, x-direction, through time is also seen Figure 10. The x-position is non-dimensionalized by the cylinder hydraulic diameter, D_h, and time, t, by the free-stream velocity, u_∞, and D_h. Vortex 1 moves a distance of $D_h \approx 0.7$ downstream by $tu_\infty/D_h \approx 3.6$, which is similar to the distance covered by vortex 2. However,

vortex 2 covers more distance for the remaining time of $D_h \approx 1.7$ versus that of $D_h \approx 1.1$ for vortex 1. Vortex 3 on the other hand can be seen to move in a linear, or constant, increase in position per time for the entire duration. Compared to vortex 1 and 2, for the first time interval discussed ($tu_\infty/D_h \approx 3.6$), vortex 3 shows the largest increase in distance of $D_h \approx 1.1$ and continues to cover a distance for the remaining time of $D_h \approx 1.7$, which is comparable to the tail end of the increase in position for vortex 2.

For comparison, DNS data showing Q-criterion structures is tracked with the same algorithm, a snapshot of which can be seen in Figure 10c. Q-criterion is defined here as the second invariant of the velocity gradient tensor, $\partial u_i/\partial x_j$, calculated from the vorticity and rate-of-strain tensors as defined by Haller [42]. While Q-criterion and dye are not visualizing the same phenomena, Q-criterion is good at showing vortex cores and is, therefore, a suitable quantity to track for comparison with the dye vortices. Due to the computational expense of DNS, the data from the simulations is limited to the region directly behind the whisker cross-section up to $3D$ downstream, where mesh stretching begins to numerically dissipate vortex structures (Figure 10d). It should also be noted that although the DNS is three-dimensional, a two-dimensional slice is analyzed and thus can only reveal motion in the streamwise direction. In contrast, the dye has engulfed multiple z-planes due to the width and diffusion of the dye, many of which are captured simultaneously by the camera image. These differences should be noted when discrepancies between methods are considered.

The two tracked vortices move in mostly linear

10

increments through time (Figure 10), although the retrieved DNS positions are much closer to the undulated geometry than the dye experiment. In fact, this is a limitation of DNS since a large computational domain is expensive, while dye experiments are limited by camera position and flow coherence.
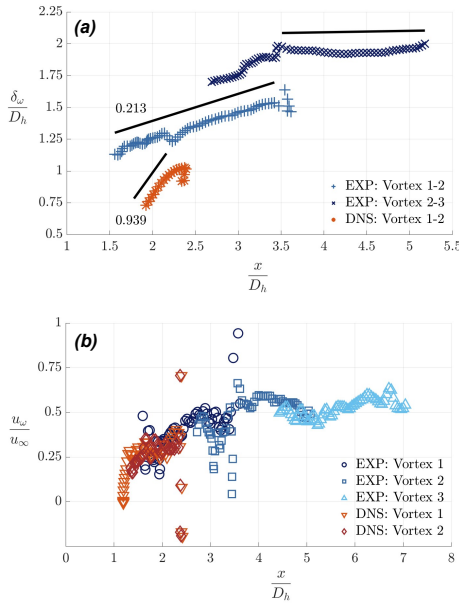
Figure 11. (a) Normalized vortex distances ($\delta_\omega/D_{\bar{h}}$) as a function of position (x/D_h) for $\lambda = 3.43$ profile and $Re = 500$. (b) Normalized vortex velocities ($u\omega/u\infty$) as a function of position (x/D_h) for $\lambda = 3.43$ profile and $Re = 500$.

To investigate the motion of the vortices further, the distance, δ_ω, between vortex 1 and vortex 2 (Vortex 1-2), and between vortex 2 and 3 (Vortex 2-3) is shown in Figure 11a. The normalized downstream distance x/D_h is referenced from the upstream vortex position from each vortex pair and δ_ω is normalized by the hydraulic diameter D_h as before. The distance between vortex 1-2 displays a sharp increase from formation to a position of $D_h \approx 3.5$ with a power of 0.21 seen in the first black linear fit in Figure 11a. Vortex 2-3 shows the same trend for values upstream of $D_h \approx 3.6$ indicating a cyclic vortical behavior. The distance between vortex 2-3, however, becomes effectively constant from $D_h \approx 3.6 - 5.2$, as seen with the downstream black linear fit in the figure, suggesting that the inter-vortex distance is steady for downstream distances beyond $D_h \approx 3.6$.

In contrast to the dye, the DNS data is limited to the near wake, and exhibits a much sharper increase from $D_h \approx 1.8 - 2.2$ than the dye results. One reason for this disparity is likely due to the different metrics employed between the Eularian Q-criterion and the Lagrangian dye tracer tracking. Another reason may be due to the CFD representation of a two-dimensional z-plane slice of the domain. This means that the

same Lagrangian particles are not necessarily captured because the dye is simultaneously diffusing through the z-planes.

From the position data, convection velocity of the vortices can be easily computed. The vortex velocities u_ω, normalized by the freestream velocity, $u\infty$, are expressed as a function of the normalized downstream position x/D_h in Figure 11b. It can be seen that there is a large initial disparity between vortex 1 and 2 velocities, with vortex 1 starting at $u_\omega/u_\infty \approx 0.24$ while vortex 2 starts out much faster at $u_\omega/u_\infty \approx 0.4$. However, vortex 1 increases in velocity significantly up to $u_\omega/u_\infty \approx 0.5$ for $D_h \approx 3$, while vortex 2 only increases to $u_\omega/u_\infty \approx 0.6$ by $D_h \approx 4.2$ and then levels off. This is consistent with the trend seen in Figure 11a, where the vortex distances become steady. More outliers are visible around this transition point of $D_h \approx 3.4$, while the velocity becomes more consistent farther downstream. Vortex 3 is seen to hold a more constant velocity throughout with minor deviations indicating a steadier state behavior.

DNS vortex 1 starts close to zero initial velocity at $D_h \approx 1.2$ and accelerates to $u_\omega/u_\infty \approx 0.24$ to match the other vorticities at the same position downstream. There is clear overlap with DNS vortex 2 and the experimental vortex 1 between x/D_h of 1.4 to 2.4. Since the the vortex velocities display good agreement, it is reasonable to attribute the slow initial velocity of DNS vortex 1 to the vortex rollup and formation above and below the geometry cross section and that the increase in velocity occurs once the vortex sheds, or detaches, from the shear layers seen in the images.

4. Conclusions

Open-source and accessible computer vision methods are used for analysis of flow over pinniped vibrissae-inspired geometry. This study is not meant to be an exhaustive study of computer vision algorithms, rather, available techniques are highlighted to show the potential speed and reliability of these methods for extraction of fundamental flow information from experimental images frames. Additional algorithms can easily be adapted to the specific needs of experimentalists beyond this study. This type of analysis allows researchers to reduce their reliance on human vision and expensive computations, which fills a middle ground often missing for experimental studies. Further specialization can include a broader range of dye tracking, wake growth quantification, or the addition of lean machine-learning algorithms.

The flow behavior observed in the qualitative observations of dye visualization reveals a clear Reynolds number dependence, specifically vortex roll-up and formation at $Re = 500$ versus oscillating

shear layer flow at $Re = 250$ for the geometry most closely resembling that of the pinniped vibrissae ($\lambda = 3.43$). The formation of coherent vortices behind the cylinder followed by downstream diffusion and mixing of the dye are also seen. Both DNS and dye visualization qualitatively reveal that the whisker topography increases spanwise flow when compared to a smooth ellipse, even at small wavelengths.

Further quantitative analysis is difficult, however, without the aid of computational methods. Two distinct computational methods were employed in this study, computer vision on the aforementioned dye images and direct numerical simulations on comparable cylindrical geometries.

Shedding frequencies for both CV and DNS methods show a consistent downward trend of the Strouhal Number (St) as a function of λ. The computer vision method outlined in background subtraction subsection is in high agreement with the DNS data and more computationally efficient for calculating the Strouhal Number for all cases below $\lambda = 6.87$. Since the wakes of the lower lambda values have continuous boundary layers present at the edges of the wake, the background subtraction method can easily find the frequencies at the wake edges, which is not the case for $\lambda = 6.87$, where that edge is not resolved due to diffusion of the dye. This suggests that the canonical $\lambda = 3.43$ geometry is optimal for reducing oscillatory frequency and therefore, vibration of the cylinder.

For this optimal $\lambda = 3.43$ case, the full power spectral density (PSD) is also extracted, and the CV method produced similar trends to that of the DNS data at a fraction of the time. The peak frequency response for the cylinders is at 0.2 for $Re = 250$, which is confirmed by both methods. DNS data for the $Re = 500$ case trend downward in a similar manner as the CV data and a dominant frequency is not discernible from the DNS data for comparison. There are peaks ranging from 0.2-0.4 suggesting a comparable frequency response with $Re = 250$ but larger amplitude variation is also present, so confirmation of peak response is unclear. What is clear is that the non-dimensional wavelength closest to biological measurements of seal whiskers ($\lambda = 3.43$) exhibited a higher degree of force reduction properties when compared other λ values.

Vorticity, Q-criterion, and critical-point calculations can be done via simulations but are computationally expensive. Tracking experimental dye vortices using simple CV techniques can be more time consuming than background subtraction depending on the K-means color quantization parameters used. However, there are several benefits of computer vision for this analysis.

Counting vortices by hand in each frame is time prohibitive and prone to human error. Tracking separate dye colors individually is not possible with DNS and the computational domain for simulations can also be limited, which means that resolving flow far down stream is usually limited. For example, in this study, the DNS data extended $x/D_h = 5$ downstream, while the dye experiment's field of view included up to $x/D_h \approx 14$.

The wide experimental field of view showed a fast increase of the vortices behind the cylinder up to the point of steady velocity. Isolating the vortices is susceptible to error if the vortices are not coherent enough or if the dye is too diffuse, but since the nature of vortices is such that they are coherent, this method is reliable and comparable to Q-criterion visualization. A full scale Re and λ comparison is, therefore, not reasonable for all the cases, since coherent vortices were not present in all cases.

For $\lambda = 3.43$, the region directly behind the cylinder has a reduction of vortex velocity, u_ω, relative to the inflow velocity u_∞ but recovers shortly by $x/D_h \approx 6.75$ where u_ω becomes steady. This behavior is further corroborated by the vortex spacing, δ_ω, which illustrates how the downstream vortices accelerate in the low pressure region behind the cylinder and catch up to each other downstream. This fast wake recovery visualized by the vortices along with their subsequent dissipation within a single frame, provides additional validation of the benefits of this undulated cylinder topography. This geometry has a wide range of application potential including industrial mixing, combustion, and chemical reactions, underwater marine applications where oscillation or vibration reduction is needed, structures that require limited wake formation, and potential improvements to bio-inspired sensors and biomimetic underwater vision [43–47].

Acknowledgments

1
2
3
4
5
6
7
8
9
10
...
60

References

[1] Hanke W, Witte M, Miersch L, Brede M, Oeffner J, Michael M, et al. Harbor seal vibrissa morphology suppresses vortex-induced vibrations. Journal of Experimental Biology. 2010 Aug;213(15):2665-72. Available from: http://jeb.biologists.org/content/213/15/2665.

[2] Witte M, Hanke W, Wieskotten S, Miersch L, Brede M, Dehnhardt G, et al. On the Wake Flow Dynamics behind Harbor Seal Vibrissae – A Fluid Mechanical Explanation for an Extraordinary Capability. In: Tropea C, Bleckmann H, editors. Results of the DFG Priority Programme 1207 "Nature-inspired Fluid Mechanics" 2006-2012. Berlin, Heidelberg: Springer; 2012. p. 271-89. Available from: https://doi.org/10.1007/978-3-642-28302-417.

[3] Hans H, Miao J, Weymouth G, Triantafyllou M. Whisker-like geometries and their force reduction properties. In: 2013 MTS/IEEE OCEANS - Bergen, Norway; 2013. p. 1-7.

[4] Wang S, Liu Y. Wake dynamics behind a seal-vibrissa-shaped cylinder: a comparative study by time-resolved particle velocimetry measurements. Experiments in Fluids. 2016 Feb;57(3). Available from: https://doi.org/10.1007/s00348-016-2117-9.

[5] Lyons K, Murphy CT, Franck JA. Flow over seal whiskers: Importance of geometric features for force and frequency response. PLOS ONE. 2020 Oct;15(10):e0241142. Available from: https://journals.plos.org/plosone/article?id=10.1371/journal.pone.0241142.

[6] Liu G, Xue Q, Zheng X. Phase-difference on seal whisker surface induces hairpin vortices in the wake to suppress force oscillation. Bioinspiration & Biomimetics. 2019 Sep;14(6). Available from: https://doi.org/10.1088%2F1748-3190%2Fab34fe.

[7] Assi GRS, Bearman PW. Vortex-induced vibration of a wavy elliptic cylinder. Journal of Fluids and Structures. 2018 Jul;80:1-21. Available from: http://www.sciencedirect.com/science/article/pii/S0889974617306382.

[8] Freymuth P. Flow visualization in fluid mechanics. Review of Scientific Instruments. 1993 Jan;64(1):1-18. Available from: https://aip.scitation.org/doi/10.1063/1.1144433.

[9] Gilpin W, Prakash VN, Prakash M. Flowtrace: simple visualization of coherent structures in biological fluid flows. Journal of Experimental Biology. 2017;220(19):3411-8.

[10] Dabiri JO, Colin SP, Costello JH, Gharib M. Flow patterns generated by oblate medusan jellyfish: field measurements and laboratory analyses. Journal of Experimental Biology. 2005;208(7):1257-65.

[11] Green MH, Ho RK, Hale ME. Movement and function of the pectoral fins of the larval zebrafish (Danio rerio) during slow swimming. Journal of Experimental Biology. 2011;214(18):3111-23.

[12] Weissburg M, Atkins L, Berkenkamp K, Mankin D. Dine or dash? Turbulence inhibits blue crab navigation in attractive–aversive odor plumes by altering signal structure encoded by the olfactory pathway. Journal of Experimental Biology. 2012;215(23):4175-82.

[13] Carr ZR, Ringuette MJ. Flow structure of low-aspect-ratio rotating wings from dye visualization. AIAA journal. 2014;52(5):1081-6.

[14] Haines GE, Sanderson SL. Integration of swimming kinematics and ram suspension feeding in a model American paddlefish, Polyodon spathula. Journal of Experimental Biology. 2017;220(23):4535-47.

[15] Raissi M, Yazdani A, Karniadakis GE. Hidden fluid mechanics: Learning velocity and pressure fields from flow visualizations. Science. 2020;367(6481):1026-30.

[16] Lu Y, Shen GX, Lai GJ. Dual leading-edge vortices on flapping wings. Journal of experimental biology. 2006;209(24):5005-16.

[17] Dabiri JO, Colin S, Katija K, Costello JH. A wake-based correlate of swimming performance and foraging behavior in seven co-occurring jellyfish species. Journal of Experimental Biology. 2010;213(8):1217-25.

[18] Sutherland KR, Madin LP. Comparative jet wake structure and swimming performance of salps. Journal of Experimental Biology. 2010;213(17):2967-75.

[19] Gerrard JH, Lighthill MJ. The wakes of cylindrical bluff bodies at low Reynolds number. Philosophical Transactions of the Royal Society of London Series A, Mathematical and Physical Sciences. 1978 Mar;288(1354):351-82. Available from: https://royalsocietypublishing.org/doi/10.1098/rsta.1978.0020.

[20] Perry AE, Chong MS, Lim TT. The vortex-shedding process behind two-dimensional bluff bodies. Journal of Fluid Mechanics. 1982 Mar;116:77-90. Available from: https://www.cambridge.org/core/journals/journal-of-fluid-mechanics/article/vortexshedding-process-behind-twodimensional-bluff-bodies/6E1ACE840A97F26223BF1F4054A08E14#.

[21] Ahmed A, Bays-Muchmore B. Transverse flow over a wavy cylinder. Physics of Fluids A: Fluid Dynamics. 1992 Sep;4(9):1959-67. Available from: https://aip.scitation.org/doi/10.1063/1.858365.

[22] Hama FR. Streaklines in a Perturbed Shear Flow. The Physics of Fluids. 1962 Jun;5(6):644-50. Available from: https://aip.scitation.org/doi/10.1063/1.1706678.

[23] Gursul I, Lusseyran D, Rockwell D. On interpretation of flow visualization of unsteady shear flows. Experiments in Fluids. 1990 Jul;9(5):257-66. Available from: https://doi.org/10.1007/BF00233126.

[24] Merzkirch W. Flow Visualization. Academic Press, New York; 1974.

[25] Karch GK, Sadlo F, Weiskopf D, Hansen CD, Li GS, Ertl T. Dye-based flow visualization. Computing in Science & Engineering. 2012;14(06):80-6.

[26] Kurada S, Rankin G, Sridhar K. Flow visualization using photochromic dyes: A review. Optics and lasers in engineering. 1994;20(3):177-92.

[27] Jobard B, Erlebacher G, Hussaini MY. Lagrangian-Eulerian advection of noise and dye textures for unsteady flow visualization. IEEE Transactions on Visualization and Computer Graphics. 2002;8(3):211-22.

[28] NELSON R. Visualization techniques for studying high angle of attack separatedvortical flows. In: 15th Aerodynamic Testing Conference; 1988. p. 2025.

[29] Delfrate JH. NASA Dryden flow visualization facility; 1995.

[30] Thu AM, Byun YH, Lee JW. Dye visualization of the vortical flow structure over a double-delta wing. Journal of Aerospace Engineering. 2012;25(4):541-6.

[31] Morrison HE, Brede M, Dehnhardt G, Leder A. Simulating the flow and trail following capabilities of harbour seal vibrissae with the Lattice Boltzmann Method. Journal of Computational Science. 2016 Nov;17:394-402. Available from: http://linkinghub.elsevier.com/retrieve/pii/S1877750316300424.

[32] Kim H, Yoon HS. Effect of the orientation of the harbor seal vibrissa based biomimetic cylinder on hydrodynamic forces and vortex induced frequency. AIP Advances. 2017 Oct;7(10). Available from: http://aip.scitation.org/doi/10.1063/1.5008658.

[33] Bradski G. The OpenCV Library. Dr Dobb's Journal of Software Tools. 2000.

[34] Arthur D, Vassilvitskii S, Gabow H. Proceedings of the eighteenth annual ACM-SIAM symposium on Discrete algorithms. Society for Industrial and Applied Mathematics. 2007.

[35] Zivkovic Z. Improved adaptive Gaussian mixture model for background subtraction. In: Proceedings of the 17th International Conference on Pattern Recognition, 2004. ICPR 2004.. vol. 2. IEEE; 2004. p. 28-31.

[36] Zivkovic Z, Van Der Heijden F. Efficient adaptive density estimation per image pixel for the task of background subtraction. Pattern recognition letters. 2006;27(7):773-80.

[37] Welch P. The use of fast Fourier transform for the estimation of power spectra: a method based on time averaging over short, modified periodograms. IEEE Transactions on audio and electroacoustics. 1967;15(2):70-3.

[38] Lyons K, Cal RB, Franck JA. Effects of wavelength on vortex structure and turbulence kinetic energy transfer of flow over undulated cylinders. Theoretical and Computational Fluid Dynamics. 2023:1-20.

[39] Weller HG, Tabor G, Jasak H, Fureby C. A tensorial approach to computational continuum mechanics using object-oriented techniques. Computers in Physics. 1998 Nov;12(6):620-31. Available from: https://aip.scitation.org/doi/abs/10.1063/1.168744.

[40] Yuasa M, Lyons K, Franck JA. Simulations of flow over a bio-inspired undulated cylinder with dynamically morphing topography. Journal of Fluids and Structures. 2022;111:103567.

[41] Liu G, Xue Q, Zheng X. Phase-difference on seal whisker surface induces hairpin vortices in the wake to suppress force oscillation. Bioinspiration & biomimetics. 2019;14(6):066001.

[42] Haller G. An objective definition of a vortex. Journal of fluid mechanics. 2005;525:1-26.

[43] y Alvarado PV, Subramaniam V, Triantafyllou M. Design of a bio-inspired whisker sensor for underwater applications. In: SENSORS, 2012 IEEE. IEEE; 2012. p. 1-4.

[44] Beem H. Seal whiskers inspire marine technology. Ocean Mag. 2016;51:82-5.

[45] Kottapalli A, Asadnia M, Hans H, Miao J, Triantafyllou M. Harbor seal inspired MEMS artificial micro-whisker sensor. In: 2014 IEEE 27th International Conference on Micro Electro Mechanical Systems (MEMS). IEEE; 2014. p. 741-4.

[46] Zheng X, Kamat AM, Cao M, Kottapalli AGP. Creating underwater vision through wavy whiskers: a review of the flow-sensing mechanisms and biomimetic potential of seal whiskers. Journal of the Royal Society Interface. 2021;18(183):20210629.

[47] Zhang X, Shan X, Xie T, Miao J, Du H, Song R. Harbor seal whisker inspired self-powered piezoelectric sensor for detecting the underwater flow angle of attack and velocity. Measurement. 2021;172:108866.

14